energy&fuels

Critical Raw Material-Free Catalysts and Electrocatalysts: Complementary Strategies to Activate Economic, Robust, and Ecofriendly SrTiO$_3$

Giovanni Carollo,* Alberto Garbujo, Fabrice Mauvy, and Antonella Glisenti*

Read Online

ACCESS | Metrics & More | Article Recommendations | Supporting Information

ABSTRACT: In this contribution, new SrTiO$_3$-based materials have been developed and their catalytic and electrocatalytic properties have been tuned by cation insertion, nanocomposition, and infiltration. The aim is to develop highly functional materials within a critical raw material-free approach with a particular aim toward durability and stability [under operating conditions of solid oxide fuel cell (SOFC) anodes] and activity toward biogas. We started from a sustainable and durable perovskite, SrTiO$_3$, with the aim of implementing performances with insertion of Ba and Mo into the crystalline cell. The catalysts are Ba$_x$Sr$_{1−x}$Ti$_{1−y}$Mo$_y$O$_3$, with $x = 0$ and 0.5 and $y = 0$, 0.1, and 0.4. Water-based wet chemistry procedures were developed specifically for each compound to obtain high purity and control barium and molybdenum insertion into the perovskite lattice. This result has been successfully obtained by means of a detailed characterization (X-ray diffraction, X-ray photoelectron spectroscopy, scanning electron microscopy, energy-dispersive X-ray spectroscopy, temperature-programmed desorption, temperature-programmed reduction, and Brunauer-EmmettTeller) carried out during each preparation steps. We demonstrated that catalytic (methane dry reforming and CO oxidation is obtained with SrTi$_{0.9}$Mo$_{0.1}$O$_3$) and electrocatalytic (of SrTi$_{0.6}$Mo$_{0.4}$O$_3$ as the anode in SOFCs) activities can be developed starting from an economic, sustainable, and robust material. Activity enhancement was obtained with nickel nanodeposition (wet impregnation and infiltration).

INTRODUCTION

Several materials exhibit high catalytic and electrocatalytic performances, mainly due to the presence of noble metals. Our aim is developing these functionalities while avoiding noble metals in a critical raw material (CRM)-free approach. To this aim, we start from sustainable but not catalytically active SrTiO$_3$ and develop catalytic and electrocatalytic performances. The target of our work is to demonstrate good catalytic activity in CO oxidation and in methane dry reforming (MDR) and the possibility to evaluate doped titanates as anodes in solid oxide fuel cell (SOFC) adding the capability to operate with C-containing fuels. Ni-based technology, in fact, is limited by the attitude of Ni toward hydrocarbons cracking and C-poisoning.

SrTiO$_3$-derived systems are characterized by good stability at high temperatures under severe reducing and oxidizing conditions, and by a low environmental and economic impact; their possible use as a superconductor[1] and photocatalyst[2,3] has already been claimed. SrTiO$_3$ is not characterized by high electrical conductivity or catalytic activity; with the present contribution, we demonstrate that these properties can be developed through a suitable insertion of cations into the perovskitic cell and building new interface active sites through nanocomposition and nanoinfiltration. We expect catalytic and electrocatalytic activity to be enhanced by inserting Mo in the B-site because of the capability of this element to create redox couples.[4−9] Mo stable oxidation state is (VI), but in a II−IV perovskite, the Mo(IV) has to prevail, so a redox couple Mo(IV)/Mo(VI) is forced. This oxidation state transition

implies passage through Mo(V) which induces the formation of electronic states inside the band gap capable of contributing to redox catalysis mechanisms.

Hence, in principle, molybdates, SrMoO$_3$ and BaMoO$_3$, besides having high electronic conductivity, are good catalysts; moreover, no significant carbon limitation poisoning is observed.[10] Molybdenum is characterized by the attitude to be stable in high oxidation state (+6); to obtain the correct phase,[11] strong reducing treatment is thus required. The consequence is a low stability of the molybdates under operating conditions.[12]

We decided for the opposite strategy: the insertion of Mo in the Ti sites (testing the effect of the increasing amount of Mo) with the aim of improving catalytic and electrocatalytic properties while maintaining the stability and robustness of SrTiO$_3$. The substitution of Ti(IV) (0.605 Å 6-coordinated[13]) with Mo(IV) should cause a crystal cell deformation (lower than in the case of Sr/Ba; Mo(IV) ionic radius when 6-coordinated is 0.65 Å) but not oxygen vacancies; the substitution of Ti(IV) with Mo(VI) (0.59 Å if 6-coordinated[13]) should not cause a significant deformation of the cell but can affect the oxidation state of titanium and the

Table 1. Thermal Treatments, Pretreatments, and Environmental Conditions Tested for Optimizing the Synthesis Procedure to Insert Mo and Ba in SrTiO$_3$; the Goldsmith Tolerance Factor (t)[5] is Also Determined Considering Both Mo(IV) and Mo(VI) to Evaluate the Difference

| Composition | Goodman tolerance factor | pretreatments | thermal treatment | | | correct phase |
			°C	environment	h	
SrTi$_{0.9}$Mo$_{0.1}$O$_3$		400 °C, 2 h air	1000	Air	6	no
		400 °C, 2 h air	850	Air	6	no
		400 °C, 2 h air	850	H$_2$	6	no
		400 °C, 2 h air	1000	5% H$_2$/Ar	6	yes with Mo impurity
		no	1000	5% H$_2$/Ar	6	yes with Mo impurity
		no	1000	20% H$_2$/Ar	6	yes with Mo impurity
		No	1000	5% H$_2$/Ar wet	6	yes with trace of impurity
		400 °C, 2 h air	1000	5% H$_2$/Ar wet	6	yes with trace of impurity
		no	1000	5% H$_2$/Ar wet	12	yes with trace of impurity
	1.006802 (100% Mo(IV)), 1.009498 (100% Mo(VI))	no	1200	5% H$_2$/Ar wet	6	yes
SrTi$_{0.6}$Mo$_{0.4}$O$_3$		no	1000	Air	6	no
		no	1000	5% H$_2$/Ar	6	yes with Mo impurity
		no	1000	5% H$_2$/Ar wet	6	yes with trace of Mo impurity
	0.999913 (100% Mo(IV)), 1.012226 (100% Mo(VI))	no	1200	5% H$_2$/Ar wet	6	yes with trace of Mo impurity
Ba$_{0.5}$Sr$_{0.5}$Ti$_{0.9}$Mo$_{0.1}$O$_3$		400 °C, 2 h air	1000	Air	6	no
		400 °C, 2 h air	1000	5% H$_2$/Ar	6	no
		400 °C, 2 h air	1000	5% H$_2$/Ar wet	6	no
		no	1000	5% H$_2$/Ar wet	6	yes with trace of Mo impurity
		no	850	5% H$_2$/Ar ethanol	6	no
		no	1000	5% H$_2$/Ar ethanol	6	yes with impurity
	0.990563 (100% Mo(IV)), 0.993605 (100% Mo(VI))	no	1000	5% H$_2$/Ar ethanol/water 50% vol	6	yes

oxygen content to maintain electroneutrality. We demonstrate in this article that cation insertion into the lattice can be used to tune ionic mobility, reducibility, and surface segregation, hence obtaining good catalysts and electrocatalysts from an almost inert perovskite. The oxygen un-balance and the Mo(IV)/Mo(VI) redox couple should allow us to develop a mixed ionic electronic conductor (MIEC), hence minimizing the triple phase boundary problems.[14]

The insertion of Ba into the lattice is usually carried out to avoid H$_2$S poisoning when using, as an example, biogas.[15] Our aim, in the present case, is to verify the conservation of the stability and its effect on ions mobility, in view of the application in SOFCs fed with real biogas. A structural deformation can be caused by the substitution of Sr (ionic radius 1.44 Å when XII coordinated[11]) with Ba(II) (1.61 Å when XII coordinated[13]) that could tune ion mobility and affect stability.

In this contribution, we developed and optimized a specific preparation procedure for each composition to obtain in-cell cation substitution avoiding segregation of undesired phases.

Further conductivity and reactivity have been reached building nanocomposites with Ni by means of wet impregnation (for catalysis application) and infiltration (for electrocatalysis application in a SOFC). Ni deposition enhances conductivity and allows the development of new active sites at the interface. CH$_4$ activation, in fact, is observed to be enhanced at the interfaces of metal/oxide.[16] Wet impregnation was preferred as a starting point for the nanocomposites because it is easy and scalable, and it allows

the deposition of the desired amount of activating materials. Eventually, infiltration was used to improve the titanate-based SOFC anode performance. The advantage of the infiltration technique is the homogeneous mixing of the cations at the low calcination temperatures required; lower temperatures allow avoiding cation interdiffusion between an electrode and electrolyte during the cell preparation and the development of net metal/MIEC oxide interfaces.[17]

Summarizing, the samples studied are:

1. SrTi$_{0.9}$Mo$_{0.1}$O$_3$ (hereafter ST9M1)
2. SrTi$_{0.6}$Mo$_{0.4}$O$_3$, (hereafter ST6M4)
3. Ba$_{0.5}$Sr$_{0.5}$Ti$_{0.9}$Mo$_{0.1}$O$_3$, (hereafter BST9M1)
4. NiO(0.3 mol)/SrTi$_{0.9}$Mo$_{0.1}$O$_3$ (Ni/ST9M1)
5. NiO(0.3 mol)/SrTi$_{0.6}$Mo$_{0.4}$O$_3$(Ni/ST6M4)

The characterization of the prepared compounds was carried out by means of X-ray diffraction (XRD), X-ray photoelectron spectroscopy (XPS), scanning electron microscopy (SEM), energy dispersive X-ray spectroscopy (EDX), BrunauerEmmettTeller, and temperature programmed reduction and desorption (TPR, TPD). The results of the characterization, with particular reference to the XRD, have been the base for the development and optimization of the synthesis procedures. The stability after cation insertion was verified both in reductive and oxidative environments. The catalytic activity was studied in two strategic probe reactions: CO oxidation and methane dry reforming (MDR); the electrocatalytic behavior was investigated testing the material as an anode of a SOFC. The possibility to address catalytic and electrocatalytic
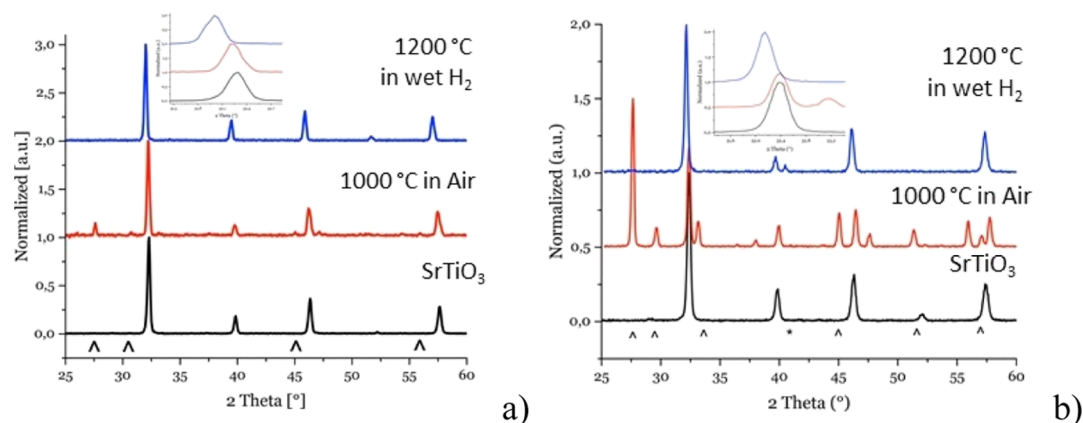
Figure 1. XRD patterns of (a) ST9M1 and (b) ST6M4 after different treatments. (^) $SrMoO_4$ (tetragonal) 01-085-0586 JCPDS database (*) Mo(0) (cubic) 00-042-1120 JCPDS database; no symbols: $SrTiO_3$ (cubic) 00-040-1500 JCPDS database.

activities by using a nanodecoration approach has been investigated considering nickel well dispersed active species.

RESULTS AND DISCUSSION: CHARACTERIZATION

Structure Investigation (XRD). The synthesis procedures have been optimized for each sample, and the effect of different reducing conditions have been evaluated (Table 1). Figure 1a displays the diffraction patterns of ST9M1. If the thermal treatment is carried out in air, an undesired insulator phase, $SrMoO_4$, forms in addition to $SrTiO_3$. This phase is observed to segregate during the synthesis at low temperatures;[18−21] to avoid its formation, specific conditions for thermal treatment have been compared and optimized (Table 1). The best result was obtained by heating in 5% H_2 + H_2O environment. Treatments in air always give rise to the insulant impurity phase, while reduction is too strong without water, favoring the formation of elemental molybdenum outside the perovskite cell. In 5% H_2 + H_2O, the insertion of Mo into the perovskite cell is confirmed by the shift toward lower values of the diffraction angles. No significant effect has the pretreatment at 400 °C carried out to gradually eliminate the organic residuals.

Also, in ST6M4 (Figure 1b) as in ST9M1, the thermal treatment in air induces the formation of $SrMoO_4$ and a treatment under reducing conditions is necessary. In this last case, the XRD pattern of ST6M4 obtained in 5% H_2 + H_2O is consistent with the formation of a small amount of Mo(0) (reflex at 40.5°).

Figure 2 shows the patterns after the thermal treatments carried out on BST9M1. The accurate optimization of pO_2 conditions is required to obtain the substitution of Sr with Ba in ST9M1; calcination in air, in fact, causes the conversion Mo(IV) → Mo(VI) and the precipitation of $BaMoO_4$, BaO, MoO_3; calcination in 5% H_2 dry conditions induces the formation of Mo(0) and a reductive treatment in 5% H_2 + H_2O induces the formation of $BaMoO_4$/BaO, MoO_3. A reductive treatment in 5% H_2 in H_2O + C_2H_5OH (50% vol) allowed us to successfully obtain the crystalline purity for $Sr_{0.5}Ba_{0.5}Ti_{0.9}Mo_{0.1}O_3$.

Stability under Oxidizing and Reducing Conditions. Once obtained the insertion of Ba and Mo inside the perovskitic crystalline cell, it is fundamental to evaluate if stability is lost. Mo(IV) is stabilized by introduction into the perovskite unit cell, and no signal is observed in the TPR curves. According to the literature,[22] titanium-based perovskites do not show any reduction peak.
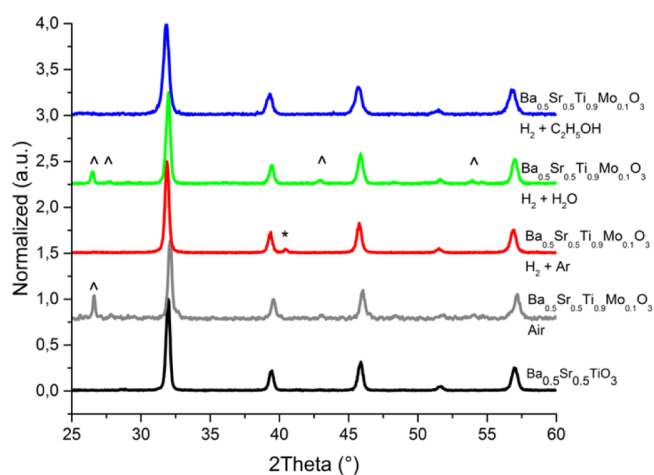
Figure 2. XRD patterns of BST9M1 obtained after the several preparation procedures. (^) $BaMoO_4$/BaO, MoO_3 (tetragonal) 00-029-0193 JCPDS database; (*) Mo(0) (cubic) 00-042-1120 JCPDS database; no symbols: $Ba_{0.5}Sr_{0.5}TiO_3$ (cubic) 00-039-0039 JCPDS database.

Bhaskar et al.[23] observed the reduction from Mo(VI) to Mo(IV) at 767 °C and the reduction of Mo(IV) to Mo(0) at 987 °C; we did not observe these contributions. The catalysts result stable also under oxidative condition: (TPO, 10% O_2/He—Figure 3).

In ST9M1, a narrow peak at 497 °C indicates the oxidation of Mo(IV) → Mo(VI) and the formation of $SrMoO_4$ (confirmed by the XRD pattern, Figure 4).

This result is in agreement with literature data (reporting oxidation at 500−700 °C).[24,25] Similar results were observed in ST6M4 and BST9M1, showing two signals at 621 and 629 °C, respectively. The higher temperatures are consistent with a stabilization of Mo(IV). The broad peak shapes could be explained by the traces of the Mo(0) on ST6M4, visible in Figure 1b at 40.5°, and by the presence of MoO_2 observed with XPS analysis which reveals the partial oxidation of Mo(IV) (confirming the stabilization), as evidenced by %O_2 consumption data. Ba greatly decreases O_2 consumption and stabilizes Mo(IV) with respect to oxidation. With respect to the total Mo, 27.9 is oxidized for BST9M1, compared with 45.3% for ST9M1 (60.9% for ST6M4). The oxidation of elemental Mo to MoO_3 also contributes to the O_2 consumption detected for ST6M4.
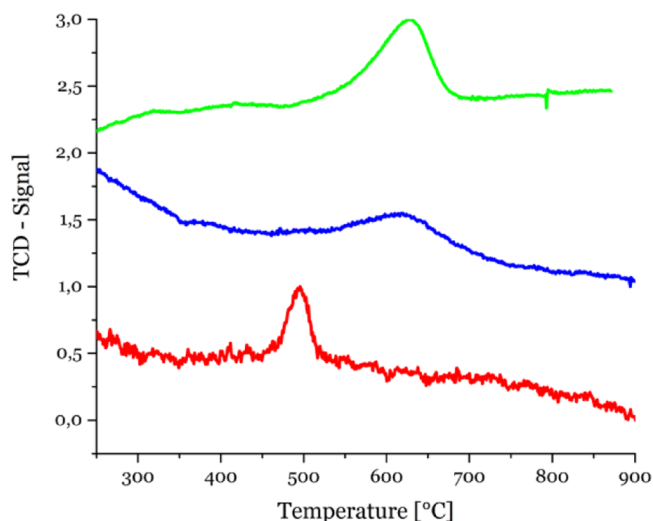
Figure 3. Temperature-programmed oxidation (TPO, 10% O_2/He) on ST9M1 (red), ST6M4 (blue), and BST9M1 (green).
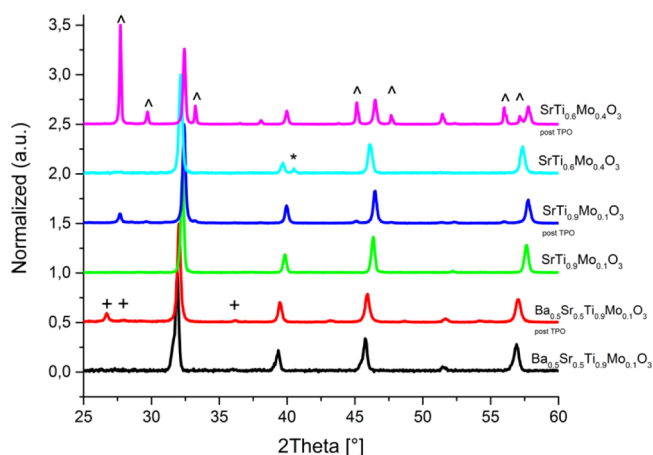
Figure 4. XRD patterns of $Ba_ySr_{1-y}Ti_xMo_{1-x}O_3$ before and after TPO (10% O_2/He). (*) Mo(0) (cubic) 00-042-1120 JCPDS database; (^) $SrMoO_4$ (tetragonal) 01-085-0586 JCPDS database; and (+) $BaMoO_4$/BaO, MoO_3 (tetragonal) 00-029-0193 JCPDS database.

The XRD patterns after TPO, Figure 4, show the presence of small amounts of $BaMoO_4$ (in BST9M1) and $SrMoO_4$ (in ST6M4 and ST9M1). With the purpose of testing the reversibility of the molybdenum oxidation, XRD study of the samples after TPR + TPO was performed and the phases were checked by XRD. ST9M1 has shown a complete structure restoration; ST6M4 and BST9M1 kept only trace of secondary phases.

The undesired phases are improbably formed during SOFC's anode working conditions (reductive) and their formation is reversible.[18−20]

Surface Characterization. Sr 3d XPS signal (Figure SI1—Supporting Information) shows contributions at 134.7−134.8 and 132.2−132.5 eV. The fitting procedure indicates the presence of the perovskites (133.8−132.2 eV) and to SrO/Sr(OH)$_2$ (133.6 and 134.9 eV for 3d$_{5/2}$ and 3d$_{3/2}$, respectively).[26−28] The Ti 2p$_{3/2}$ XPS peak position 458.6−458.4 eV (Figure SI1) corresponds to cations in $SrTiO_3$ and $BaTiO_3$.[27] Sample BST9M1 shows a contribution at 460.5 eV (Figure SI1) that is consistent with a higher hydroxylation. The asymmetric Ba 3d$_{5/2}$ (Figure SI1) is at 779.4 eV as

expected for Ba in $BaTiO_3$. Small contributions of $BaCO_3$ (typically at 779.1 eV) and $Ba(OH)_2$ (779.3 eV) are observed.[29,30]

Considering both Mo(VI) (235.5−235.6 eV) and Mo(IV) (232.5 eV), the Mo(VI)/Mo(IV) ratio is 0.7 in ST9M1 (0.85 in ST6M4) and 2.0 in BST9M1. The surface segregation of Mo(VI) is not due to the effect of barium on the structure stability (the Goldschmidt tolerance factor is only very slightly affected by the presence of barium—Table 1—and is very near to the unity value, independently on the oxidation state of Mo) but to the different preparation conditions.[31−33] It deserves to be underlined that XPS results are not conflicting with TPR ones. At first it is evident from the XPS signal that Mo(IV) is the main species, considering, moreover, that, in the present case (Al Kα anode—detection angle 45°), the sampling depth of Mo 3d signal is from 7 to 8 nm suggesting very few monolayers of Mo(VI), not enough to be observed in the TPR curve.

Two species contribute to the oxygen signal: lattice oxygen (529.6 eV) and hydroxyl groups (about 531.8 eV) such as $Ba(OH)_2$ and non-perovskitic oxides (MoO_3 and TiO_2) on the surface.[32−36]

The XPS quantitative analysis of Mo-doped titanates is reported in Table 2. For a comparison, the samples $SrTiO_3$ and $Sr_{0.5}Ba_{0.5}TiO_3$ were prepared trough citrates' synthesis and treated under the same reductive atmosphere used for Mo-doped titanates. All the samples are characterized by surface oxygen over stoichiometry confirming the presence of OH-terminations. This is relevant because OH-groups can evolve into Lewis surface active acidic and basic sites under thermal treatment. Lewis surface sites can enhance CO and CO_2 coordination eventually increasing the reactivity.[37] In Table 2, also the cations-only surface compositions (at. %) are reported to underline the surface segregation phenomena. Ti surface segregation in $SrTiO_3$ is observed to be less evident when Mo is inserted. In this case, Sr is surface segregated in the sample with a lower amount of Mo, whereas Mo tends to surface segregate when present in higher amounts. A similar trend is observed also in the Ba-containing samples but is a lot less evident: the presence of large ion Ba^{2+} in BST9M1 keeps the cation concentration close to the nominal value. Surface segregation causes the creation of highly defective interfaces that play a significant role in molecule activation (see Paragraph 3.1).

Yoo et al.[38] underline the equal mobility of constituent cations in $BaTiO_3$ and thus the absence of compositional demising. Studies carried out on $Ba_{1-x}Sr_xTiO_3$ perovskites suggested similar mobility for Ba and Ti and a higher mobility for Sr.[38−40] However, the lower constrain in the crystal structure can be considered.[13] The insertion of Ba into the cell causes the decrease of ion mobility. Mo/Ti atomic ratios for BST9M1 and ST9M1 are lower than the expected ones being 0.07 and 0.08, respectively. In ST6M4, a more significant surface segregation of Mo was detected. The cation mobility in doped $BaTiO_3$ was related, by Rahaman et al.,[41] to the presence of dopants with attitude as donors (increased mobility) and acceptor (decreased mobility). In this case, the relative amount of Mo(VI)-donor/Mo(IV)-not donor seems not to play a role confirming that Mo(VI) is not inserted into the perovskite cell but segregated as oxide and cannot affect bulk diffusion. The substitution of Ti with Mo seems to slightly reduce the amount of surface oxygen whose atomic % gets closer to the nominal one. This is not observed in the sample

Table 2. XPS Atomic Composition Obtained for the before and after the Insertion of Ba and Mo into the Perovskitic Cell and for the Ni-Activated Nanocomposites[a]

sample		Ni	Ba	Sr	Ti	Mo	O	Mo/Ti	Sr/Ti	O/(Sr + Ti + Mo)
$Ba_{0.5}Sr_{0.5}Ti_{0.9}Mo_{0.1}O_3$	XPS		6	7	14	1	72	0.07	0.50	2.57
			21	25	49	4				
	nominal		10	10	18	2	60	0.11	0.56	1.50
			25	25	45	5				
$SrTi_{0.9}Mo_{0.1}O_3$	XPS			18	12	1	69	0.08	1.50	2.26
				58	40	2				
	nominal			20	18	2	60	0.11	1.11	1.50
				50	45	5				
$SrTi_{0.6}Mo_{0.4}O_3$	XPS			17	8	8	67	1.00	2.13	2.0
				52	24	24				
	nominal			20	12	8	60	0.67	1.67	1.50
				50	30	20				
$SrTiO_3$	XPS			23	13		64		1.77	1.78
				63	37					
	nominal			20	20		60		1.00	1.50
				50	50					
$Sr_{0.5}Ba_{0.5}TiO_3$	XPS		6	8	14		72		0.57	2.57
			20	29	51					
	Nominal		10	10	20		60		0.50	1.50
			25	25	50					
$Ni/SrTi_{0.9}Mo_{0.1}O_3$	XPS	10		13	6	1	72	0.17	2.17	2.57
		36		41	21	2				
	nominal	7		17	15	2	59	0.13	1.13	1.44
		18		41	37	4				
$Ni/SrTi_{0.6}Mo_{0.4}O_3$	XPS	8		12	5	5	71	1.00	2.40	2.45
		29		36	17	17				
	nominal	7		17	10	7	59	0.70	1.70	1.44
		18		41	25	16				

[a]The nominal compositions, derived from the weighted amounts, are reported for comparison. The atomic compositions determined considering only the cations are indicated below the corresponding O-containing ones. This choice allows us to emphasize the surface segregation phenomena hidden by the relevant amount of oxygen.

containing Barium; this result underlines the significant role of Ba in surface hydroxylation and the minor role of Ti.

The SEM images (Supporting Information—Figure SI2) reveal an homogeneous globular morphology composed by particles of 100−200 nm diameter, probably as a consequence of the high temperatures involved during the synthesis.

The specific surface area (between 4 and 5 m²/g) seems not to be particularly affected by the synthesis conditions. The particle size distributions displayed the presence of two main diameters, 4 and 0.5 μm (Supporting Information—Figure SI3). The d(0.5) of ST9M1 and ST6M4 was 4.014 and 4.200 μm, respectively.

■ RESULTS AND DISCUSSION: CATALYTIC AND ELECTROCATALYTIC BEHAVIOR

Enhancing Catalytic Activity by Doping: Reactivity with CO + O₂. $SrTiO_3$ is not active in CO oxidation or in dry reforming,[42] whereas after insertion of dopants, the almost total CO conversion (Figure 5a) is observed at 700−800 °C (operative conditions of SOFCs). The total CO conversion is reached by ST6M4 at 800 °C, and ST9M1 at the same temperature achieved 93%, thus underlying the effect of Mo on catalytic activity. BST9M1 has shown the lower CO conversion (80%). The ignition temperature follows the order ST9M1 < ST6M4 < BST9M1 (Figure SI4) and a sort of plateau is observed in ST9M1 (400−500 °C) and ST6M4 (600−700 °C), that is the temperature range observed for Mo(IV) →

Mo(VI), Figure 3, confirming the essential role of oxygen. In agreement with the Mars van Krevelen mechanism,[5,43,44] CO is oxidized by lattice oxygen which is successively restored by added oxygen. The preparation conditions (reduction) induce a subsurface oxygen depletion which is recovered when the temperature allowed it; similarly, the catalytic activity is recovered.

A relevant contribution is also due to the surface active oxygen species responsible, at the lower temperature, for a suprafacial mechanism. For undoped and doped $LaCoO_3$, Pinto and Glisenti[45] observed the prevalence of the suprafacial versus intrafacial mechanism until 350 °C. The suprafacial activation is probably un-favoured by the stability of Mo(VI). Intrafacial activation can be relevant at high temperatures. The compound with the higher amount of Mo, which is characterized by the larger oxygen consumption (see TPO results), is the catalyst showing the greater improvement in performance.

The lower performance was observed on BST9M1 (starting temperature 500 °C), but no activation step is needed. This is in agreement with the minor oxygen consumption and lower oxygen mobility of BST9M1 which makes difficult the subsurface oxygen deficiency correction. Low mobility at the grain boundaries can contribute to the low oxygen mobility. Reduced grain boundaries mobility has been observed by several authors and confirmed to be enhanced by aliovalent doping.[42]
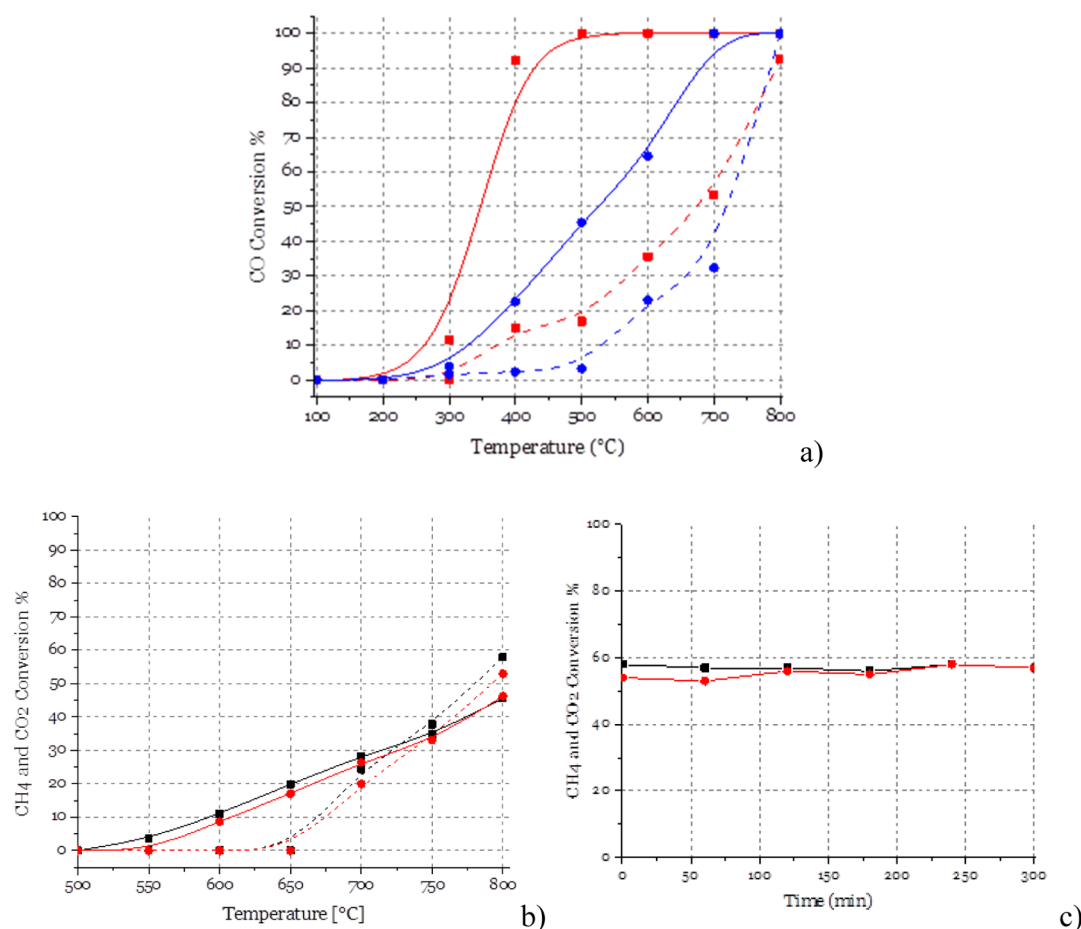
Figure 5. (a) CO conversion as a function of temperature for ST9M1 (red), ST6M4 (blue), before (dotted line) and after (continuous line) Ni-deposition. (b) ST9M1: % conversion in $CH_4 + CO_2$ from 500 to 800 °C. CH_4 (black) and CO_2 (red); before (dotted line) and after (continuous line) Ni-deposition. (c) ST9M1: % conversion in $CH_4 + CO_2$ (stoichiometric) at 800 °C for 300 min. CH_4 (black) and CO_2 (red).

Enhancing Catalytic Activity by Doping: Dry Reforming. MDR is an endothermic reaction of high scientific and industrial importance that requires very high temperatures.[46−49] In spite of being studied from 1888, it is not yet considered an industrially mature process, also because of the C-poisoning and sintering of the catalysts.

All catalysts have been tested, but only ST9M1 shows some activity (58% of CH_4 and 53% of CO_2 conversion at 800 °C), Figure 5b. The activity started at around 625 °C, and the conversion increases linearly with temperature. The catalyst was kept at 800 °C under working condition for 6 h without showing decrease of catalytic performance (Figure 5c).

Several aspects affect the performances of catalyst: the strong interaction between supporting and active phases, the dispersion and size of active phase, the basicity, the reducibility, the oxygen exchange capability, porosity, and specific surface area.[50] The mechanism of MDR has been investigated on several catalysts.[51−53] In general, four steps are considered: (1) dissociative adsorption of methane: which is the rate-determining step and should be favored by step active sites; (2) dissociative adsorption of CO_2, which is generally considered fast particularly at the metal-support interface. (3) Hydroxyl groups formation; and (4) Intermediate oxidation and desorption: surface oxygen is considered responsible of the conversion of CH_x-groups adsorbed on the surface in CO and H_2.

The reactivity of the ST9M1 can be explained by considering the surface composition. Polo-Garzon et al.[54] observed a marked effect of the perovskite surface composition and segregation phenomena on catalytic activity. In particular, they investigated the interaction and activation of methane on several $SrTiO_3$ samples obtained by means of different preparation procedures and subjected to different post-synthetic treatments. The obtained results, supported by DFT calculations, indicate that the concentration of Sr at the top layers is proportional to the rate of methane combustion; DFT simulations showed that Sr step surfaces provide the lowest activation barrier for methane dissociation. In the present case, XPS indicated the higher atomic % of Sr are in ST9M1 and ST6M4 (18 and 17%, respectively). This suggests that, besides Sr, Mo also plays a role. By means of a NAPPES study, Reddy et al. observed reversible changes in the electronic structure of Mo-oxides, related with the presence of Mo(V) necessary to assure the co-existence of Mo(IV) and Mo(VI) and capable of originating now electronic states below the Fermi energy, with marked effect on catalytic and electrocatalytic behavior.[55] These states could contribute to the weakening of the C−H bond. Consistently with literature data, the fitting procedure (results in Supporting Information) allows us to reveal the presence of Mo(IV) and Mo(V); in ST9M1, the Mo(IV)−Mo(V)/Mo(VI) atomic ratio is around 1, whereas in ST6M4, it is 0.1, and only Mo(VI) is observed in BST9M1. In ST6M4, molybdenum is mainly segregated

pubs.acs.org/EF

outside the perovskitic cell as Mo(VI) and cannot contribute to C−H bond activation. Surface-segregated Mo(VI) greatly decreases the catalytic activity as a consequence of the stability of this oxidation state and/or the absence of active exposed facets.[56,57] Another role surely played by Mo is decreasing the C-poisoning: the anti-coking effect of this element was observed, as an example, by Siahvashi et al. in the propane dry reforming[58] and by Neofytidis et al. in an SOFC operating with methane internal reforming.[59]

Enhancing Reactivity through Nickel Deposition. The effect of Ni deposition was investigated only in the catalysts without Ba because of the marked decrease of the catalytic performance consequent to this doping. The aim of the development and study of the Ni (0.3 mol %)/$SrTi_{1−x}Mo_xO_3$ nanocomposites is to exploit the synergy between Ni and Mo at the interface; in particular, the idea is to make use of the attitude of Mo to bind oxygen to help keeping Ni in an elemental state. This should be helpful both for catalysis activity and conductivity (fundamental in SOFC electrodes).

TPR analysis is consistent with the deposition of 0.28 and 0.30 mol/mol, respectively, for Ni/ST9M1 and Ni/ST6M4. The signals are centered at 400 and 550 °C (Figure SI5) and correspond to the reduction of Ni(II) poorly (400 °C) and strongly (550 °C) interacting with Ti and/or Mo.[60−63] A contribution due to Mo(VI) reduction can be excluded comparing the experimental and nominal hydrogen consumption values and the low temperature (the reduction MoO_3 was observed to be promoted by Ni around 640−650 °C[64,65]). The amount of Ni on the surface (XPS, Table 2) is higher than the nominal one in Ni/ST9M1 and almost corresponding to the nominal one in Ni/ST6M4; the quantitative results suggest the absence of diffusion toward bulk, the peak positions correspond to Ni(II). Ni deposition does not affect the Mo/Ti atomic ratio but causes a slight increment of Sr. Oxygen was detected in high amounts [O/(Sr + Ti + Mo) atomic ratio increases from 2.2 to 2.6].

The deposition of 30% mol/mol of Ni greatly increases the catalytic activity in CO oxidation (Figure 5a): the ignition temperature of Ni/ST9M1 is reduced more than 100 °C and achieved total CO conversion at 500 °C; Ni/ST6M4 shows an ignition temperature around 200 °C and is able to reach the total CO conversion at 700 °C. Both the catalysts did not display the intermediate temperature plateau suggesting that oxygen lacking is not a limiting step. This agrees with capability of Ni to facilitate CO chemisorption. CO is observed to adsorb molecularly on Ni obtained by reduction of a NiO(100) surface; CO_2 forms by means of the lattice oxygen of the supporting perovskite, following the Mars van Krevelen mechanism. Oxygen vacancies thus generated themselves as active sites for coordination of CO.[59] The higher performance of Ni/ST9M1 is consistent with a higher capability of the support surface, rich of molybdenum in lower oxidation states, to bind oxygen avoiding the oxidation of Ni.

Among all Ni-containing catalysts, only Ni/ST9M1 showed reactivity in methane dry reforming, Figure 5b. Ni impregnation does not increase the total CH_4 conversion but shifts the starting temperature to 500 °C. The results underline that the addition of Ni improves the catalytic activity by allowing the methane and carbon dioxide molecules activation at lower temperatures.[48,52,56,66] Following above-mentioned mechanisms, the CO_2 activation can be due to the deposited Ni and the CH_4 activation to the Ni/perovskite interface. Also, in this case, the presence of molybdenum in lower oxidation

states is precious for assuring catalytic performance, as already mentioned.

The catalyst was kept working at 800 °C 6 h showing only a small decrease in the conversion after the first hour, 41% CH_4 and 38% CO_2. Further work is in course to verify the durability and the amount of surface carbon as a function of the reaction conditions[46,50,56,57,66,67] and the de-coking action of molybdenum.[68]

Enhancing Electrochemical Performance by Ni Infiltration. The electrochemical investigation was carried out on ST9M1, Ni/ST9M1, and Ni/ST6M4. The choice is driven by the results obtained in the catalytic tests (CO oxidation and dry reforming) in which the Ba-doped compound exhibits the lower performance. The amount of Ni is 15% wt. The symmetric SOFCs are the following:

ST9M1/GDC/YSZ/GDC/ST9M1
Ni/ST9M1/GDC/YSZ/GDC/Ni/ST9M1
Ni/ST6M4/GDC/YSZ/GDC/Ni/ST6M4

The tests have been carried out in anode conditions (H_2 5% in Ar).

The GDC buffer layer was necessary to avoid ion diffusion and improve compatibility between the electrolyte (YSZ) and the electrode (see Supporting Information—Figure SI6).

Figure 6 shows the homogeneous distribution of Ni particles on the final pellets backbone of ST9M1 and ST6M4. ST6M4 is
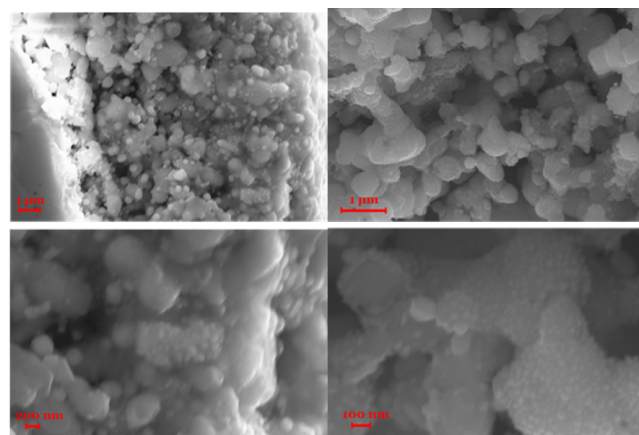
Figure 6. SEM images of Ni/ST9M1 (left upper and lower for different magnifications) and Ni/ST6M4 (right upper and lower for different magnification) treated at 1300 °C.

characterized by a more significant porosity and smaller Ni particle diameters (average diameter is 20−30 nm) compared with ST9M1 (about 100 nm particle diameters).

Area specific resistance (ASR) (area specific resistance = $(R_pS)/2$ with R_p = polarization resistance and S = surface area of the electrode) values have been obtained by Nyquist plots through a model circuit fitting, an example of which is reported in Figure 7.

The fitting of the experimental data was carried out by means of Zview software (Scribner associated) using the more adequate equivalent circuits; the relations, 1 and 2,[69] allowed us to calculate the frequency relaxation, f_r, and the equivalent capacitance of each contribution, C_{eq}

$$f_r = 1/[2\pi(R \times CPE)^{1/n}] \tag{1}$$

where R = resistance, [CPE] = module of CPE, n = dispersion parameter.
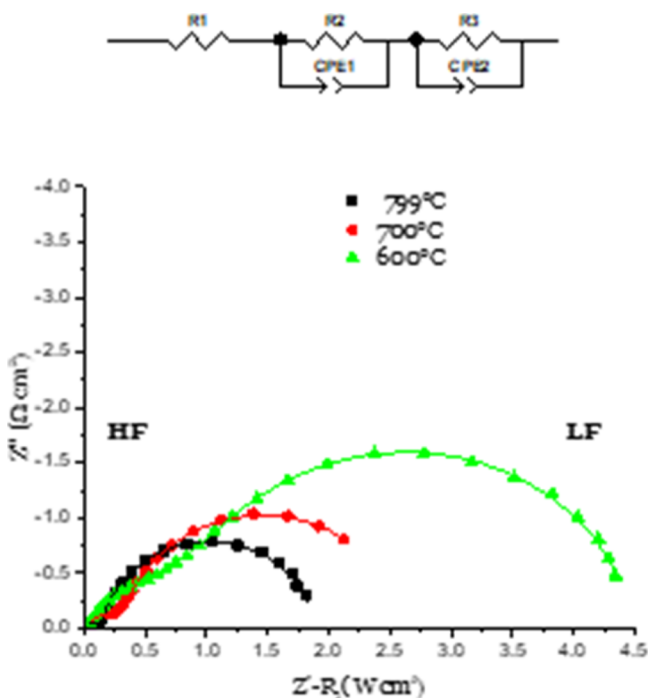
Figure 7. Nyquist plot of Ni/ST6M4 at 600 °C (green), 700 °C (red), and 799 °C (black) under 100 cm³/min of H_2 5% in argon.

$$C_{eq} = R^{[(1-n)n]} \times CPE^{(1/n)} \tag{2}$$

In Figure 8, it is reported that the behavior of ASR versus temperature (from 500 to 830 °C) for the samples ST9M1,
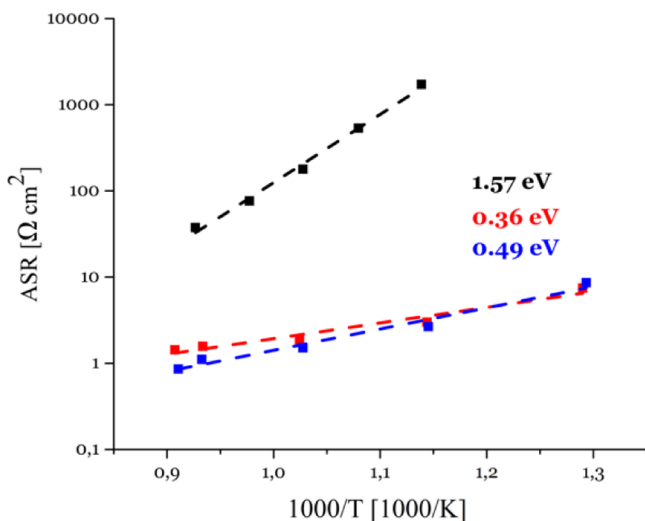
Figure 8. ASR Arrhenius plot for ST9M1 (black), Ni/ST9M1 (red), and Ni/ST6M4 (blue). The activation energy values obtained by fitting these data are also reported.

Ni/ST9M1 and Ni/ST6M4. ST6M4 infiltrated with 15% wt Ni gave the better performance (0.85 Ω cm² at 830 °C). The value greatly decreases after Ni infiltration (from 27.2 Ω cm²) and is lower than the ASR determined for Ni/ST9M1 (1.42 Ω cm²). Ni infiltration decreases the E_a for ST9M1 from 1.57 to 0.36 eV (better than the E_a determined for Ni/ST6M4—0.49 eV).

Ni/ST9M1 and Ni/ST6M4 impedance spectra were fitted to calculate the capacitance of each contribution, C_e, a necessary step for attributing processes.[69]

The data obtained are consisting with two processes contributing to limit the cell performance. These processes can be attributed, based on the corresponding capacitance values (Figure 9), to electrode processes (the contribution of the electrolyte is characterized by lower capacitances).[69−71]
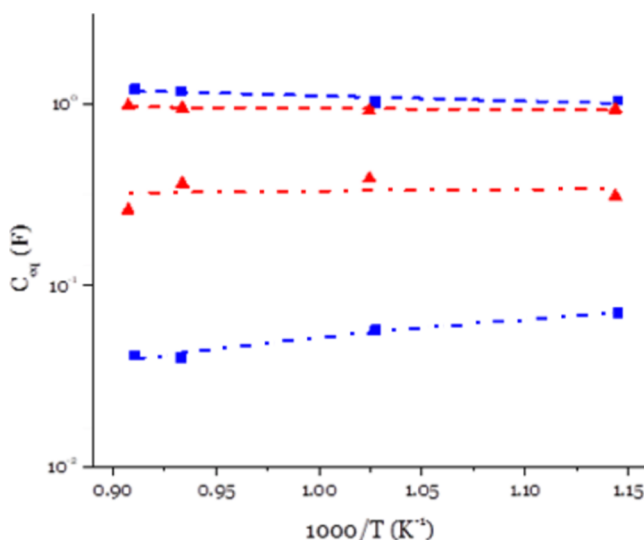
Figure 9. Arrhenius plot of the capacitances for Ni/ST9M1 (red) and Ni/ST6M4 (blue). Dash-dot lines refer to the process at low capacity, and dash lines refer to the process at high capacity.

The comparison with the literature suggests that their origin is in the modest electrocatalytic capability of titanates.[70,71] The two processes are attributed to the reactions that occurred on three phase boundaries Ni/backbone (smaller contribution) and on the perovskites surface (larger contribution).

The significant decrease of the contribution at lower capacitance (0.1 F) suggests to attribute it to the catalytic activity developed at the interface Ni/perovskite. In fact, the Ni dispersion is higher in Ni/ST6M4 with respect to Ni/ST9M1 (Figure 6), whereas the amount of deposited Ni is the same. The other contribution is probably due to the microstructure; it does not change as a function of the Ni-dispersion, perovskite composition, or temperature.

■ CONCLUSIONS

In this work, new CRM-free SrTiO₃-based materials were developed and optimized to obtain good catalytic and electrocatalytic activity. These properties have been created by three approaches: the substitution of lattice Sr and Ti cations with Ba and Mo, the nano-composition by deposition of Ni, and the Ni infiltration.

The developed materials have been tested as catalysts in CO oxidation and MDR, possible fuels in SOFCs. The ions substitution into the crystalline cells produces both its deformation and the creation of a Mo(IV)/Mo(VI) redox couple; these phenomena allows us to tune the ion mobility, mixed ionic electronic conduction, and catalytic activity. The catalytic performance in the above-mentioned reactions suggested the possibility to use these materials as an anode for SOFCs fed with C-containing fuels.

High crystalline purity on all the compounds required an accurate optimization of the pO_2 pressure conditions. The stability tests (TPR/TPO) performed on sample powders have confirmed that cation substitution does not affect stability.

All materials are active in CO oxidation under SOFCs' working temperature condition (total CO conversion for ST6M4, 93% for ST9M1 and 80% for BST9M1). ST9M1 shows a good activity in MDR (58% of CH_4 and 53% of CO_2 conversion at 800 °C), and no significant decrease in reactivity is observed. The activity is attributed to a synergic effect between Ti and Mo. To increase the catalytic activity, nickel deposition (30% mol) on ST9M1 and ST6M4 was carried out. CO oxidation greatly increases. Ni/ST9M1 shows an ignition temperature drop (from 650 to 500 °C) in MDR.

Impedance electrochemical spectroscopy demonstrated the feasibility to use ST6M4 infiltrated with 15 wt % with nickel as the anode for SOFCs: an ASR of 0.85 Ω cm^2, was achieved at 830 °C.

Summarizing, good catalytic activity can be obtained by substituting 10% at. of Ti with Mo, while electrocatalytic activity is higher when 40% at.of Ti is substituted. Ni improves both the catalytic (impregnation) and electrocatalytic (infiltration) performance. Because of the beneficial effect of the Ni/perovskite interface, further work is in course for the development of Ni nanoparticles deposition procedures that allow us to assure a better control on the distribution and size.

ASSOCIATED CONTENT

Ⓢ Supporting Information

The Supporting Information is available free of charge at https://pubs.acs.org/doi/10.1021/acs.energyfuels.0c01678.

> Synthesis condition for perovskites and nanocomposites, XPS spectra, TPR graphs of the composites, XRD patterns illustrating the compatibility between the electrode and different electrolytes (GDC and YSZ), SEM images of the perovskites and the particle size, different steps for SOFC realization and testing, and catalytic activity in CO oxidation of all the samples (PDF)

AUTHOR INFORMATION

Corresponding Authors

Giovanni Carollo — *Department of Chemical Sciences, University of Padova, 35131 Padova, Italy*; Phone: +39 0498275858; Email: giovanni.carollo.1@phd.unipd.it

Antonella Glisenti — *Department of Chemical Sciences, University of Padova, 35131 Padova, Italy; CNR—ICMATE, 35131 Padova, Italy*; ⓞ orcid.org/0000-0003-4334-2150; Phone: +39 049 8275176; Email: antonella.glisenti@unipd.it

Authors

Alberto Garbujo — *Department of Chemical Sciences, University of Padova, 35131 Padova, Italy*

Fabrice Mauvy — *CNRS—Université de Bordeaux, ICMCB, F-33608 Pessac Cedex, France*

Complete contact information is available at:
https://pubs.acs.org/10.1021/acs.energyfuels.0c01678

Notes

The authors declare no competing financial interest.

REFERENCES

(1) Collignon, C.; Lin, X.; Rischau, C. W.; Fauque, B.; Behnia, K.; Sachdev, S.; Marchetti, M. C. Metallicity and Superconductivity in Doped Strontium Titanate. *Annu. Rev. Condens. Matter Phys.* **2019**, *10*, 25−44.

(2) Adnan, M. A. B.; Arifin, K.; Minggu, L. J.; Kassim, M. B. Titanate-based perovskites for photochemical and photoelectrochemical water splitting applications: A review. *Int. J. Hydrogen Energy* **2018**, *43*, 23209−23220.

(3) Chiang, T. H.; Lyu, H.; Takashi, H.; Yosuke, G.; Tsuyoshi, T.; Masao, K.; Tsutomu, M.; Kazunari, D. Efficient Photocatalytic Water Splitting Using Al-Doped SrTiO$_3$ Coloaded with Molybdenum Oxide and Rhodium−Chromium Oxide. *ACS Catal.* **2018**, *8*, 2782−2788.

(4) Tejuca, L. G.; Fierro, J. L. G.; Tascón, J. M. D. Structure and reactivity of perovskite-type oxides. *Adv. Catal.* **1989**, *36*, 237−328.

(5) Peña, M. A.; Fierro, J. L. G. Chemical Structures and Performance of Perovskitic oxides. *Chem. Rev.* **2001**, *101*, 1981−2018.

(6) Savaniu, C. D.; Irvine, J. T. S. La-doped SrTiO$_3$ as anode material for IT-SOFC. *Solid State Ionics* **2011**, *192*, 491−493.

(7) Gorte, R. J.; Kim, H.; Vohs, J. M. Novel SOFC Anodes for the Direct Electrochemical Oxidation of Hydrocarbons. *J. Power Sources* **2002**, *106*, 10−15.

(8) Orera, A.; Slater, P. R. New chemical systems for solid oxide fuel cells. *Chem. Mater.* **2010**, *22*, 675−690.

(9) Yi, F.; Li, H.; Chen, H.; Zhao, R.; Jiang, X. Preparation and characterization of La and Cr co-doped SrTiO$_3$ materials for SOFC anode. *Ceram. Int.* **2013**, *39*, 347−352.

(10) Hou, X.; Marin-Flores, O.; Kwon, B. W.; Kim, J.; Norton, M. G.; Ha, S. Gasoline-fueled solid oxide fuel cell with high power density. *J. Power Sources* **2014**, *268*, 546−549.

(11) Marrero-López, D.; Peña-Martínez, J.; Ruiz-Morales, J. C.; Martín-Sedeño, M. C.; Núñez, P. High temperature phase transition in SOFC anodes based on Sr$_2$MgMoO$_{6-\delta}$. *J. Solid State Chem.* **2009**, *182*, 1027−1034.

(12) Vincent, A.; Luo, J.-L.; Chuang, K. T.; Sanger, A. R. Effect of Ba doping on performance of LST as anode in solid oxide fuel cells. *J. Power Sources* **2010**, *195*, 769−774.

(13) Shannon, R. D. Revised effective ionic radii and systematic studies of interatomic distances in halides and chalcogenides. *Acta Crystallogr., Sect. A: Cryst. Phys., Diffr., Theor. Gen. Crystallogr.* **1976**, *32*, 751−767.

(14) He, B.; Wang, Z.; Zhao, L.; Pan, X.; Wu, X.; Xia, C. Ti-doped molybdenum-based perovskites as anodes for solid oxide fuel cells. *J. Power Sources* **2013**, *241*, 627−633.

(15) Adler, S. B. Factors governing oxygen reduction in solid oxide fuel cell cathodes. *Chem. Rev.* **2004**, *104*, 4791−4844.

(16) Samorjai, G. A. *Introduction to Surface Chemistry and Catalysis*, 1st ed.; Wiley, 1994.

(17) Graves, C.; Martinez, L.; Sudireddy, B. R. High performance nano-ceria electrodes for solid oxide cells. *ECS Trans.* **2016**, *72*, 183−192.

(18) Vasala, S.; Yamauchi, H.; Karppinen, M. Role of SrMoO$_4$ in Sr$_2$MgMoO$_6$ synthesis. *J. Solid State Chem.* **2011**, *184*, 1312−1317.

(19) dos Santos-Gómez, L.; León-Reina, L.; Porras-Vázquez, J. M.; Losilla, E. R.; Marrero-López, D. Chemical stability and compatibility of double perovskite anode materials for SOFCs. *Solid State Ionics* **2013**, *239*, 1−7.

(20) Marrero-López, D.; Peña-Martínez, J.; Ruiz-Morales, J. C.; Gabás, M.; Núñez, P.; Aranda, M. A. G.; Ramos-Barrado, J. R. Redox behaviour, chemical compatibility and electrochemical performance of Sr$_2$MgMoO$_{6-\delta}$ as SOFC anode. *Solid State Ionics* **2010**, *180*, 1672−1682.

(21) Yang, L. C.; Gao, Q. S.; Tang, Y.; Wu, Y. P.; Holze, R. MoO$_2$ synthesized by reduction of MoO$_3$ with ethanol vapour as an anode material with good rate capability for the lithium ion battery. *J. Power Sources* **2008**, *179*, 357−360.

(22) Takehira, K.; Shishido, T.; Kondo, M. Partial Oxidation of CH$_4$ over Ni/SrTiO$_3$ Catalysts Prepared by a Solid-Phase Crystallization Method. *J. Catal.* **2002**, *207*, 307−316.

(23) Bhaskar, T.; Reddy, K. R.; Kumar, C. P.; Murthy, M. R. V. S.; Chary, K. V. R. Characterization and reactivity of molybdenum oxide catalysts supported on zirconia. *Appl. Catal., A* **2001**, *211*, 189−201.

(24) Kubo, J.; Ueda, W. Catalytic behaviour of AMoO$_x$ (A = Ba, Sr) in oxidation of 2-propanol. *Mater. Res. Bull.* **2009**, *44*, 906−912.

(25) Martínez-Coronado, R.; Alonso, J. A.; Aguadero, A.; Fernández-Díaz, M. T. New SrMo$_{1-x}$Cr$_x$O$_{3-\delta}$ perovskites as anodes in solid-oxide fuel cells. *Int. J. Hydrogen Energy* **2014**, *39*, 4067−4073.

(26) Ura, B.; Trawczyński, J.; Kotarba, A.; Bieniasz, W.; Illán-Gómez, M. J.; Bueno-López, A.; López-Suárez, F. E. Effect of potassium addition on catalytic activity of SrTiO$_3$ catalyst for diesel soot combustion. *Appl. Catal., B* **2011**, *101*, 169−175.

(27) Yang, W.-D. X-ray photoelectron spectroscopy and electrical properties studies of La$_2$O$_3$ -doped strontium titanate ceramics prepared by sol-precipitation method. *J. Mater. Sci.* **1999**, *4*, 3533−3544.

(28) Nagarkar, P. V.; Searson, P. C.; Gealy, F. D. Effect of surface treatment on SrTiO$_3$: An x-ray photoelectron spectroscopic study. *J. Appl. Phys.* **1991**, *69*, 459−462.

(29) Tsunekawa, S.; Ito, S.; Mori, T.; Ishikawa, K.; Li, Z.-Q.; Kawazoe, Y. Critical size and anomalous lattice expansion in nanocrystalline BaTiO$_3$ particles. *Phys. Rev. B: Condens. Matter Mater. Phys.* **2000**, *62*, 3065−3070.

(30) Wegmann, M.; Watson, L.; Hendry, A. XPS Analysis of Submicrometer Barium Titanate Powder. *J. Am. Ceram. Soc.* **2004**, *87*, 371−377.

(31) Ellefson, C. A.; Marin-Flores, O.; Ha, S.; Norton, M. G. Synthesis and applications of molybdenum (IV) oxide. *J. Mater. Sci.* **2012**, *47*, 2057−2071.

(32) Li, J.; Lv, T.; Hou, N.; Li, P.; Yao, X.; Fan, L.; Gan, T.; Zhao, Y.; Li, Y. Molybdenum substitution at the B-site of lanthanum strontium titanate anodes for solid oxide fuel cells. *Int. J. Hydrogen Energy* **2017**, *42*, 22294.

(33) Choi, J.-G.; Thompson, L. T. XPS study of as-prepared and reduced molybdenum oxides. *Appl. Surf. Sci.* **1996**, *93*, 143−149.

(34) Verhoeven, J. A. T.; Van Doveren, H. An XPS investigation of the interaction of CH$_4$, C$_2$H$_2$, C$_2$H$_4$ and C$_2$H$_6$ with a barium surface. *Surf. Sci.* **1982**, *123*, 369−383.

(35) Hanawa, T.; Ota, M. Calcium phosphate naturally formed on titanium in electrolyte solution. *Biomaterials* **1991**, *12*, 767−774.

(36) Zou, J.; Schrader, G. L. Multicomponent Thin Film Molybdate Catalysts for the Selective Oxidation of 1,3-Butadiene. *J. Catal.* **1996**, *161*, 667−686.

(37) Kung, H. H. *Transition Metal Oxides: Surface Chemistry and Catalysis*; Elsevier: Amsterdam, 1989; Chapter 5.

(38) Yoo, H.-I.; Lee, C.-E.; De Souza, R. A.; Martin, M. Equal mobility of constituent cations in BaTiO$_3$. *Appl. Phys. Lett.* **2008**, *92*, 252103.

(39) Lee, C.; Yoo, H. Ba/Ti ratio effect on oxygen re-equilibration kinetics of donor-doped BaTiO3. *Solid State Ionics* **2008**, *179*, 338−346.

(40) Saha, S.; Krupanidhi, S. B. Microstructure related influence on the electrical properties of pulsed laser ablated (Ba,Sr)TiO$_3$ thin films. *J. Appl. Phys.* **2000**, *88*, 3506−3513.

(41) Rahaman, M. N.; Manalert, R. Grain Boundary Mobility of BaTiO$_3$ doped with Aliovalent Cations. *J. Eur. Ceram. Soc.* **1998**, *18*, 1063−1071.

(42) Glisenti, A.; Natile, M. M.; Carlotto, S.; Vittadini, A. Co- and Cu-Doped Titanates: Toward a New Generation of Catalytic Converters. *Catal. Lett.* **2014**, *144*, 1466−1471.

(43) Royer, S.; Duprez, D.; Kaliaguine, S. Oxygen mobility in LaCoO$_3$ perovskites. *Catal. Today* **2006**, *112*, 99−102.

(44) Mars, P.; van Krevelen, D. W. Oxidations carried out by means of vanadium oxide catalysts. *Chem. Eng. Sci.* **1954**, *3*, 41−59.

(45) Pinto, D.; Glisenti, A. Pulsed reactivity on LaCoO$_3$-based perovskites: a comprehensive approach to go inside CO oxidation mechanism and the effect of dopants. *Catal.: Sci. Technol.* **2019**, *9*, 2749−2757.

(46) Pakhare, D.; Spivey, J. A review of dry (CO$_2$) reforming of methane over noble metal catalysts. *Chem. Soc. Rev.* **2014**, *43*, 7813−7837.

(47) Jang, W.-J.; Shim, J.-O.; Kim, H.-M.; Yoo, S.-Y.; Roh, H.-S. A review on dry reforming of methane in aspect of catalytic properties. *Catal. Today* **2019**, *324*, 15−26.

(48) Wang, Y.; Yao, L.; Wang, S.; Mao, D.; Hu, C. Low-temperature catalytic CO$_2$ dry reforming of methane on Ni-based catalysts: a review. *Fuel Process. Technol.* **2018**, *169*, 199−206.

(49) Aramouni, N. A. K.; Touma, J. G.; Tarboush, B. A.; Zeaiter, J.; Ahmad, M. N. Catalyst design for dry reforming of methane: analysis review. *Renewable Sustainable Energy Rev.* **2018**, *82*, 2570−2585.

(50) Jang, W.-J.; Shim, J.-O.; Kim, H.-M.; Yoo, S.-Y.; Roh, H.-S. A review on dry reforming of methane in aspect of catalytic properties. *Catal. Today* **2019**, *324*, 15−26.

(51) Papadopoulou, C.; Matralis, H.; Verykios, X. *Utilization of Biogas as a Renewable Carbon Source: Dry Reforming of Methane in Catalysis for Alternative Energy Generation*; Guczi, L., Erdöhelyi, A., Eds.; Springer: New York, 2012; pp 57−127.

(52) Kumar, N.; Kanitkar, S.; Wang, Z.; Haynes, D.; Shekhawat, D.; Spivey, J. J. Dry reforming of methane with isotopic gas mixture over Ni-based pyrochlore catalyst. *Int. J. Hydrogen Energy* **2019**, *44*, 4167−4176.

(53) Bachiller-Baeza, B.; Mateos-Pedrero, C.; Soria, M. A.; Guerrero-Ruiz, A.; Rodemerck, U.; Rodríguez-Ramos, I. Transient studies of low-temperature dry reforming of methane over Ni-CaO/ZrO$_2$-La$_2$O$_3$. *Appl. Catal., B* **2013**, *129*, 450−459.

(54) Polo-Garzon, F.; Fung, V.; Liu, X.; Hood, Z. D.; Bickel, E. E.; Bai, L.; Tian, H.; Foo, G. S.; Chi, M.; Jiang, D.-e.; Wu, Z. Understanding the Impact of surface reconstruction of perovskite catalysts on CH$_4$ activation and combustion. *ACS Catal.* **2018**, *8*, 10306−10315.

(55) Reddy, K. P.; Mhamane, N. B.; Ghosalya, M. K.; Gopinath, C. S. Mapping valence band and interface electronic structure changes during the oxidation of Mo to MoO$_3$ via MoO$_2$ and MoO$_3$ to MoO$_2$: a NAPPES study. *J. Phys. Chem. C* **2018**, *122*, 23034−23044.

(56) Yao, L.; Galvez, M. E.; Hu, C.; Da Costa, P. Mo-promoted Ni/Al$_2$O$_3$ catalyst for dry reforming of methane. *Int. J. Hydrogen Energy* **2017**, *42*, 23500−23507.

(57) Henrich, V. E.; Cox, P. A. *The Surface Science of Metal Oxides*; Cambridge University Press, 1996; Chapter 6.

(58) Siahvashi, A.; Chesterfield, D.; Adesina, A. A. Propane CO$_2$ (dry) reforming over bimetallic Mo-Ni/Al$_2$O$_3$ catalyst. *Chem. Eng. Sci.* **2013**, *93*, 313−325.

(59) Neofytidis, C.; Dracopoulos, V.; Neophytides, S. G.; Niakolas, D. K. Electrocatalytic performance and carbon tolerance of ternary Au-Mo-Ni/GDC SOFC anodes under CH$_4$-rich Internal Steam Reforming conditions. *Catal. Today* **2018**, *310*, 157−165.

(60) Li, C.; Chen, Y.-W. Temperature-programmed-reduction studies of nickel oxide/alumina catalysts: effects of the preparation method. *Thermochim. Acta* **1995**, *256*, 457−465.

(61) Hadjiivanov, K.; Mihaylov, M.; Abadjieva, N.; Klissurski, D. Characterization of Ni/TiO2 catalysts prepared by successive adsorption−reduction of Ni2+ ions. *J. Chem. Soc., Faraday Trans.* **1998**, *94*, 3711−3716.

(62) Jing, Q.; Loua, H.; Feia, J.; Houa, Z.; Zheng, X. Syngas production from reforming of methane with CO$_2$ and O$_2$ over Ni/SrO−SiO$_2$ catalysts in a fluidized bed reactor. *Int. J. Hydrogen Energy* **2004**, *29*, 1245−1251.

(63) Chettibi, S.; Keghouche, N.; Benguedouar, Y.; Bettahar, M. M.; Belloni, J. Structural and Catalytic Characterization of Radiation-Induced Ni/TiO$_2$ Nanoparticles. *Catal. Lett.* **2013**, *143*, 1166−1174.

(64) Afanasev, P. V.; Tsurov, M. A.; Kostyuk, B. G.; Turakulova, A. O.; Lunin, V. V. Interactions in the NiO-MoO$_3$ system upon reduction. *Kinet. Catal.* **1993**, *34*, 490−492.

(65) Zhang, J.; Li, C.; Guan, W.; Chen, X.; Chen, X.; Tsang, C.-W.; Liang, C. Promotional effect of Co and Ni on MoO$_3$ catalysts for hydrogenolysis of dibenzofuran to biphenyl under atmospheric hydrogen pressure. *J. Catal.* **2020**, *383*, 311−321.

(66) Kwon, B. W.; Oh, J. H.; Kim, G. S.; Yoon, S. P.; Han, J.; Nam, S. W.; Ham, H. C. The novel perovskite-type Ni-doped Sr$_{0.92}$Y$_{0.08}$TiO$_3$ catalyst as a reforming biogas (CH$_4$+CO$_2$) for H$_2$ production. *Appl. Energy* **2018**, *227*, 213−219.

(67) Usman, M.; Wan Daud, W. M. A.; Abbas, H. F. Dry reforming of methane: Influence of process parameters - A review. *Renew. Sustain. Energy Rev.* **2015**, *45*, 710−744.

(68) Pérez-Camacho, M. N.; Abu-Dahrieh, J.; Goguet, A.; Sun, K.; Rooney, D. Self-cleaning perovskite type catalysts for the dry reforming of methane. *Chin. J. Catal.* **2014**, *35*, 1337−1346.

(69) Dailly, J.; Fourcade, S.; Largeteau, A.; Mauvy, F.; Grenier, J. C.; Marrony, M. Perovskite and A$_2$MO$_4$-type oxides as new cathode materials for protonic solid oxide fuel cells. *Electrochim. Acta* **2010**, *55*, 5847−5853.

(70) Du, Z.; Zhao, H.; Yang, C.; Shen, Y.; Yan, C.; Zhang, Y. Optimization of strontium molybdate based composite anode for solid oxide fuel cells. *J. Power Sources* **2015**, *274*, 568−574.

(71) Zho, X.; Yan, N.; Chuang, K. T.; Luo, J. L. Progress in La-doped SrTiO$_3$ (LST)-based anode materials for solid oxide fuel cells. *RSC Adv.* **2014**, *4*, 118−131.